Quantum behavior of terahertz photoconductivity in silicon nanocrystals networks

V. Pushkarev,[1] T. Ostatnický,[2] H. Němec,[1] T. Chlouba,[2] F. Trojánek,[2] P. Malý,[2] M. Zacharias,[3]
S. Gutsch,[3] D. Hiller,[3] and P. Kužel[1,*]

[1]*Institute of Physics ASCR, Na Slovance 2, 18221 Prague 8, Czech Republic*
[2]*Faculty of Mathematics and Physics, Charles University in Prague, Ke Karlovu 3, 12116 Prague 2, Czech Republic*
[3]*IMTEK Faculty of Engineering, Albert-Ludwigs-University of Freiburg, Georges-Köhler-Allee 103, 79110 Freiburg, Germany*

Quantum-size effects are essential for understanding the terahertz conductivity of semiconductor nanocrystals, particularly at low temperatures. We derived a quantum mechanical expression for the linear terahertz response of nanocrystals; its introduction into an appropriate effective medium model provides a comprehensive microscopic approach for the analysis of terahertz conductivity spectra as a function of frequency, temperature, and excitation fluence. We performed optical pump–terahertz probe experiments in multilayer Si quantum dot networks with various degrees of percolation at 300 and 20 K and with variable pump fluence (initial carrier density) over nearly three orders of magnitude. Our theoretical approach was successfully applied to quantitatively interpret all the measured data within a single model. A careful data analysis made it possible to assess the distribution of sizes of nanocrystals participating to the photoconduction. We show and justify that such conductivity-weighted distribution may differ from the size distribution obtained by standard analysis of transmission electron microscopy images.

I. INTRODUCTION

Optoelectronic properties of semiconductor nanostructures can be tuned and optimized by their composition, size, and surface properties, which are fundamentally influenced by fabrication methods and by postgrowth treatment such as passivation of interfaces. Silicon nanocrystals (NCs) [1] possess properties that find applications in various fields, including photovoltaics [2], optoelectronics [3], and biosensing [4]. Confinement of the charge carriers inside nanostructures, their transport among individual nano-elements, and the interface-related electronic processes carry growing importance for these applications. Deep understanding of the band structure, luminescent properties, and charge carrier transport in NCs and NC networks, namely in correlation with technological steps during the material preparation, can further increase their application potential. The terahertz (THz) spectral range has great potential to address fundamental questions relevant to these fields as well as the related applications: THz probing provides access to the pertinent length scales, allowing the description of the charge carrier transport in nanostructures; it also greatly helps to target material properties important for the nanoelectronics and provides feedback for the fabrication technologies.

Time-resolved THz spectroscopy provides a useful mean to assess the motion of optically injected carriers inside NCs as well as the charge transport among NCs on an ultrafast time scale, i.e., it provides information about the conductive quality of individual NCs and about their size, connectivity, and morphology, including, namely, the percolation degree. The Si NCs prepared by thermal decomposition of SiO_x layers have been extensively studied in the past by THz spectroscopic techniques. First, the THz conductivity spectra of thick layers (~ 0.2–$1\ \mu$m; $0.2 \leqslant x \leqslant 1.4$) containing randomly distributed

Si NCs were interpreted within the framework of phenomenological Drude-Smith model [5–7]. Note that these samples are characterized by a broad size distribution and complex NCs networking in all three dimensions. A better control over the NC size and filling fraction is obtained in multilayers composed of ultrathin SiO_x/SiO_2 bilayers [8,9]; nevertheless, it has been shown by THz conductivity measurements [10] that even in this case the NCs form a non-negligible amount of larger clusters and aggregates with more or less mutually interconnected NCs. The broad distribution of NC sizes and namely the complex morphological structures of these materials make the quantitative microscopic interpretation of the measured transient THz spectra quite challenging. The transmission electron microscopy (TEM) images enable detection of NCs with the most frequently represented sizes in the sample; these NCs are typically nanometer sized in thermally decomposed SiO_x layers. The THz photoconductivity spectra are more sensitive to larger nano-objects [10]: They then provide a complementary picture of the distribution of larger NCs and of more complex NC networks that are hardly resolved in the TEM pictures.

In this paper, we study the THz conductivity of Si NCs prepared by thermal decomposition of SiO_x/SiO_2 bilayers. It turns out that the THz conductivity behavior at low temperatures (LTs) can be explained only by assuming the quantum behavior of electrons inside NCs. Our advanced analysis then allows us to determine microscopic parameters of the samples, namely the distribution of sizes of NCs that participate to the conductive response of SiO_x layers. This is put into relation with the size distribution determined by TEM.

Indeed, quantum effects such as discretization of energy levels and the corresponding appearance of resonances in the far infrared spectra are expected in nanometer-sized NCs. For this reason, interpretation of the experimental data within the framework of classical theories without direct incorporation of quantum effects may be questionable. We therefore develop a quantum model of NC conductivity in the THz spectral range,

* kuzelp@fzu.cz

125424-1

TABLE I. Summary of sample properties from the literature and from optical and THz measurements presented in this paper.

Sample	$x = 0.0$	$x = 0.3$	$x = 0.5$	$x = 0.7$	Comment
Si areal fill fraction s_A (%)	$\sim$100	$\sim$100	63	38	From EF-TEM (Ref. [12])
Si volumetric fill fraction s (%)	99	84			From measured optical absorption[a]
			42	25	$s = 2/3\ s_A$
n of NC layers at 400 nm	5.4	4.1	2.4	2.0	From effective medium calculations[b]
α at 400 nm (cm^{-1})	8.6×10^4	3.7×10^4	0.72×10^4	0.35×10^4	From effective medium calculations[b]
α at 400 nm (cm^{-1})	12×10^4	5.5×10^4	1.7×10^4	0.30×10^4	From optical absorbance measurements (Fig. 1)
s_{coh}(%)	54	22	14	1.2	Fit of THz data
s_{inc}(%)	44	29	3	<0.1	Fit of THz data
K_{inc}	$\gtrsim$20	2	2		Fit of THz data
μ_{RT} (cm^2 V^{-1} s^{-1})	30	18	15		Fit of THz data
μ_{LT} (cm^2 V^{-1} s^{-1})	10	10	6		Fit of THz data
Conductive NCs (%)	$\sim$100	60	40	<5	$= (s_{coh} + s_{inc})/s$

[a]The volumetric filling fraction s was calculated from the areal filling fraction ($s = 2/3\ s_A$) for samples with $x = 0.5, 0.7$. For sample SiO$_{0.3}$, the value was chosen in order to match the experimental and theoretical optical absorbance in Fig. 1. For SiO$_{0.0}$, the value should be close to 100%: For $s = 99$%, we obtain again a good match between the experimental and theoretical optical absorbance.

[b]The procedure of calculation of effective refractive index and absorption coefficient in the optical range was described in Ref. [10]; the complex refractive index of pure Si was taken from Ref. [14]: ($\alpha_{Si} = 9.5 \times 10^4$ cm^{-1}, $n_{Si} = 5.55$).

and we use it to interpret the experimental data. The agreement between the theory and experiment at both room temperature (RT) and LTs underlines the high relevance of the model.

The paper is organized as follows. In Sec. II, we provide information regarding sample preparation and regarding the experimental techniques used. In Sec. III, we set up the theoretical model. We develop the quantum mechanical calculations of the THz mobility of carriers (Sec. III A), and we introduce the calculated mobility into an appropriate effective medium theory reflecting the inhomogeneous nature of the samples (Sec. III B). Based on this formalism, a global model of transient THz transmittance spectra is developed, and we illustrate how the size of NCs influences various THz spectra (Sec. III C). In Sec. IV, we describe the fitting procedure, and we compare the fits to the experimental data. Finally, in Sec. V, we conclude, emphasizing important implications for interpretation of THz spectra of semiconductor nanostructures.

II. EXPERIMENTAL DETAILS

A. Samples: preparation and preliminary characterization

The studied nanocrystalline Si superlattice samples are similar to those reported in Ref. [10] but prepared using improved technological steps [nitrogen-free SiO$_x$ plasma enhanced chemical vapor deposition (PECVD) process]. The samples are composed of 100 bilayers consisting of a 4.5-nm-thick layer, which contains Si NCs in SiO$_2$ environment, and of a 4-nm-thick isolating layer of SiO$_2$. The sample preparation is described in detail in Ref. [11]. Basically, a periodic SiO$_x$/SiO$_2$ structure was prepared by means of the SiH$_4$ + O$_2$ + Ar PECVD process. Subsequently, these structures underwent a thermal annealing at 1100 °C for 1 hour in pure N$_2$, which induced phase separation between silicon and silicon dioxide in the silicon-rich layers and the crystallization of Si NCs. The samples were finally at 500 °C annealed in a pure H$_2$ atmosphere to passivate the dangling bond defects at the Si/SiO$_2$ interfaces.

Adjustment of the precursor gas flow ratio in PECVD allowed reaching a wide variety of the silicon oxide composition (we focused on samples with $x = 0.7, 0.5, 0.3,$ and 0.0): The amount of Si excess in the initial SiO$_x$ layers controls the size of Si NCs as well as their volumetric filling factor s within each layer. The sample with $x = 0.0$ corresponds to a polycrystalline silicon layer.

Selected properties of the samples published previously or measured in this paper are summarized in Table I. The size distribution of NCs and the filling factor in our samples were determined by plane-view energy-filtered TEM (EF-TEM) [12]. The average size of NCs in sample SiO$_{0.7}$, as determined by EF-TEM, is 5.0 ± 1.5 nm in relation with the nominal thickness of SiO$_x$ layers. The EF-TEM images indicate that silicon in the samples SiO$_{0.5}$, SiO$_{0.3}$, and SiO$_{0.0}$ is percolated and that the average size of Si NCs is thus an undefined quantity from this point of view. On the other hand, we show in Sec. IV that the THz photoconductivity spectra strikingly depend on the pump fluence (i.e., on the photocarrier concentration). It has been shown and extensively discussed that such a finding is a fundamental signature of a significant contribution to the conductivity of inclusions that are not electrically percolated [10,19,20,23]. This apparent discrepancy between TEM and THz measurements will be thoroughly discussed at the end of this paper. At this point, we stress the reason why we systematically develop here a description in terms of the quantum confinement of photocarriers in isolated NCs.

Optical absorbance at the pump wavelength is a crucial parameter for the analysis of transient THz spectra. In Fig. 1, we show the absorbance of our samples at 400 nm, and we compare it with effective absorbance of the Si/SiO$_2$ mixture calculated using a Maxwell-Garnett effective medium approximation [10] and the transfer-matrix formalism for layered structures [13]. To this aim, we used the intrinsic optical properties of silicon (absorption coefficient $\alpha_{Si} = 9.5 \times 10^4$ cm^{-1}, refractive index $n = 5.55$) [14]. There is a reasonable agreement between these data sets, which corroborates the view that the samples are composed mainly
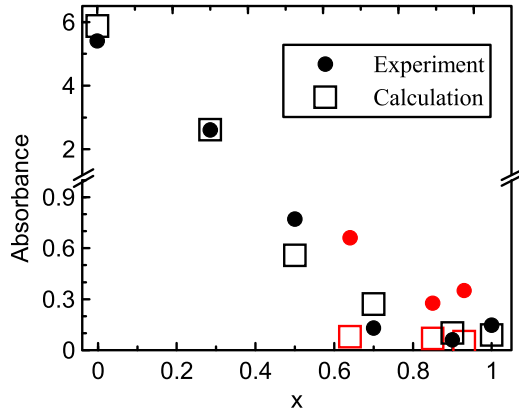
FIG. 1. Calculated and measured optical absorbance of various Si NC samples at 400 nm defined as $-\ln(I_s/I_{sub})$, where I_s is the transmitted light intensity through the sample (including all internal reflections in the layered structure) and I_{sub} is the transmitted intensity through the bare substrate. Black symbols: samples investigated in this paper; red symbols: similar samples with extrinsic absorption on incorporated nitrogen investigated previously in Ref. [10].

of Si and SiO_2 and that they are free of extrinsic absorption. From this analysis, we also conclude that the quantum yield ξ of the photogeneration of mobile carriers is close to one in these samples. This is in contrast with the former samples from [10]: Those samples exhibited a considerably higher absorbance, which was ascribed to extrinsic absorption due to a high amount of incorporated nitrogen from using N_2O gas instead of O_2 in the PECVD [8,10].

B. The THz photoconductivity measurements

Measurements of the transient THz photoconductivity spectra (optical pump–THz probe experiments) were performed using a conventional setup for time-resolved THz spectroscopy [15] driven by Ti:sapphire ultrafast regenerative laser amplifier (Spitfire ACE, central wavelength 800 nm, 1 mJ pulse energy, 5 kHz repetition rate). A part of the output laser beam was frequency doubled to 400 nm (3.1 eV) and subsequently used for the sample photoexcitation. Homogeneous excitation across the sample was achieved by defocusing of the beam to an area significantly larger than the diameter of the aperture of the metallic sample holder; the pump beam fluence was controlled over nearly three orders of magnitude using a combination of neutral density filters and a variable attenuator based on a thin film polarizer. Another part of the laser beam was used for the THz pulse generation, detection via optical rectification, and electro-optic sampling in 1-mm-thick ZnTe crystals. The THz pulses impinged on the sample under normal incidence, thus probing the charge transport in the plane of the sample. The experiments were performed at RT and at 20 K in a liquid helium continuous flow cryostat (Optistat CF).

The photoconductivity spectra were measured at a pump-probe delay of 10 ps, i.e., at a significantly shorter delay than the exciton formation time [16]. For this reason, we do not consider the electron-hole interaction, and we interpret our results in the frame of conduction band carrier motion.

III. THz SPECTRAL RESPONSE

Two effects play an important role in the THz photoconductivity spectra of semiconductor nanostructures: charge confinement inside nanostructures and depolarization fields [17]. In our past publications, we used semiclassical Monte-Carlo simulations [18] to assess the former effect and effective medium theory based on the Bergman approach [19,20] to take into account properly the latter one. This was also the case in similar Si NC multilayers [10], where we studied entirely nonpercolated samples, and the model provided very nice quantitative agreement with the experiment at RT by using nominal sample parameters (i.e., without fitting).

This approach fails in a comparison of the photoconductivity spectra of our currently studied Si NCs at RT and LTs. On one hand, the morphology of the sample does not change with temperature; therefore, the effective medium model should be temperature independent. On the other hand, the semiclassical Monte-Carlo simulations predict quite dramatic changes in the microscopic conductivity and consequently in the THz transmission spectra, e.g., higher values of the microscopic mobility and a significant redshift of the conductivity peak of confined carriers have been previously predicted for bandlike transport in microcrystalline silicon upon cooling [15]. However, such effects are not confirmed experimentally in the current paper. In fact, the spectra measured at 20 and 300 K do not differ much.

For this reason, we develop quantum mechanical calculations of the THz conductivity. At RT, the quantum model provides the same spectra as the semiclassical approach, but the results significantly differ at LTs. Namely, the quantum calculations are able to reproduce the experimental photoconductivity spectra.

In Sec. III A, we develop a model of quantum mechanical THz conductivity of a single isolated NC, and in Sec. III B we introduce it into the context of effective medium response of nonpercolated and percolated structures. Finally, in Sec. III C we consider the THz response of an ensemble of NCs with a broad distribution of sizes.

A. Quantum mechanical model of the THz conductivity

We describe the system of a confined electron probed by external electric field $E(\omega)$ within the density matrix formalism, which permits us to account for its incoherent evolution. The total density matrix is defined as $\rho = \rho_0 + \rho^{(1)}$, where ρ_0 describes the thermal equilibrium state of the system (unperturbed by external fields) and $\rho^{(1)}$ is the first-order perturbation caused by the field $E(\omega)$. The Liouville equation within the first-order perturbation theory,

$$i\hbar\dot{\rho}^{(1)} = [H_0,\rho^{(1)}] + [H',\rho_0] - i\hbar\gamma\rho^{(1)}, \qquad (1)$$

phenomenologically introduces a decoherence due to the inelastic scattering of electrons through the dephasing rate γ (note that γ formally describes both the pure dephasing and the carrier population decay). The total Hamiltonian H was decomposed to its unperturbed part H_0 and the linear perturbation H' by the electromagnetic field $H = H_0 + H'$. For simplicity, we consider the NCs as infinitely deep three-dimensional (3D) rectangular potential wells. The unperturbed Hamiltonian satisfies the stationary Schrödinger equation

$H_0|k\rangle = \hbar\omega_k|k\rangle$, where the multi-index k denotes a bound state in the potential well. Since the NCs are much smaller than the wavelength of THz radiation, we use the dipole approximation to describe the interaction of electrons with the external electric field: $H' = -e\mathbf{r} \cdot \mathbf{E}(\omega)$. The frequency-dependent electron mobility is defined as

$$\mu(\omega) = j(\omega)/eNE(\omega), \qquad (2)$$

where e is the electron charge, N is the electron density, and $j(\omega)$ denotes the electric current density as a linear response to $E(\omega)$. In the first-order perturbation theory, the current density reads

$$\mathbf{j}(\omega) = \frac{e}{V_0} \frac{\partial}{\partial t} \langle x \rangle = \frac{e}{V_0} \frac{\partial}{\partial t} \mathrm{Tr}[\rho^{(1)}\mathbf{r}], \qquad (3)$$

where V_0 is the system volume, m is the electron effective mass, and $\mathbf{r}$ is the quantum-mechanical operator of position. We set $(\partial/\partial t) = -i\omega$ in order to evaluate the stationary solution of Eq. (1) at a given frequency ω,

$$\langle k|\rho^{(1)}|l\rangle = \frac{eE(\omega)x_{kl}}{\hbar} \frac{f_k - f_l}{\omega - \omega_k + \omega_l + i\gamma}, \qquad (4)$$

where the mean population of the level k is given by the Fermi-Dirac distribution $f_k = \langle k|\rho_0|k\rangle$ and where $x_{kl} = \langle k|x|l\rangle$ is the dipole matrix element (assuming that the field is polarized along the x direction). The resulting formula for the mobility then stems from Eqs. (2) and (3):

$$\mu(\omega) = -\frac{i\omega e}{n} \sum_{kl} \frac{f_k - f_l}{\hbar} \frac{|x_{kl}|^2}{\omega - \omega_k + \omega_l + i\gamma}. \qquad (5)$$

Here $n = \sum_k f_k$ is the mean number of electrons per NC (in our calculations, we typically choose $n \ll 1$).

Note that Eq. (5) significantly differs from the expression derived from the Kubo formula (see, e.g., Ref. [21] or Eq. (25) in Ref. [22]), which is widely used for electronic systems excited at optical frequencies. Indeed, the Kubo formula and Eq. (5) provide the same spectra in the optical, near-, and mid-infrared regimes (provided that $\omega \gg \gamma$); however, the mobility given by Eq. (25) in Ref. [22] does not vanish for $\omega = 0$. This is because it does not account for all electric currents in confined systems and its application should be limited to frequencies $\omega > \gamma$. In contrast, the mobility calculated with the help of Eq. (5) drops to zero in the DC regime (i.e., electrons localized in a NC cannot drift away) and can be used to interpret the THz conductivity spectra in semiconductor NCs where usually $\omega \lesssim \gamma$.

In the calculations of quantum mechanical conductivity spectra, we considered NCs in the form of rectangular boxes with dimensions $a_x \times a_y \times a_z$ and an infinite confining potential. Assumption of the infinite depth of the potential well is best justified by comparing the electron band offset between Si and SiO$_2$ ($\sim$3.1 eV) and the energy of electron states that contribute to the THz response (well below 0.5 eV). The choice of the particular shape of the confining potential allowed us to perform complex numerical calculations within a reasonable time: Indeed, the shape of real NCs in the sample is irregular, and we expect that the differences in the response of NCs of different shapes do not exceed the experimental error as long as their characteristic dimensions and symmetries are similar. We checked this assumption numerically by comparing the

rectangular and spherical potentials. The dimension a_z is perpendicular to the layers, and it is constrained by the sample geometry to values smaller than the nominal layer thickness of 4.5 nm. Consequently, to calculate spectra of NCs larger than 4 nm, we assume that a_x and a_y can take any required values, while a_z is fixed to 4 nm. The calculations of eigenstates of unperturbed Hamiltonian take into account the anisotropy of the conduction band minima in the L valley of silicon (effective masses: $m_1 = m_2 = 0.19, m_3 = 0.97$). The position of the strongest resonance in the microscopic mobility spectra depends on the temperature and electron density in the NC since they determine which dipole transition between the energy levels becomes the most pronounced. At low electron density (less than one electron per NC), the largest contribution comes from the transition from the ground to the first excited state, thus resulting in a resonance at frequency $3\hbar^2\pi^2/2m_0m_1a_x^2 \approx$ 240 meV (57 THz) for NC size $a_x = 5$ nm, 27 meV (6.6 THz) for $a_x = 15$ nm, and 9 meV (2.4 THz) for $a_x = 25$ nm. Here m_0 denotes the free electron mass.

The mean carrier concentration used in the calculations corresponds to less than one photoelectron per NC. In this case, the vast majority of NCs is either unexcited or occupied by a single electron; therefore, the Pauli exclusion principle has a negligible influence and the thermal Fermi-Dirac distribution of electrons can be approximated by the Maxwell-Boltzmann distribution function, as we verified for our particular system. In this regime, the mobility is independent of the carrier concentration.

In Fig. 2, we present examples of calculated microscopic mobility spectra in the THz and multi-THz range. Clearly, we observe a dependence of the spectrum on the NC size. The main part of the signal (peaks corresponding to transitions between quantum energy levels) occurs in the multi-THz range for the NC sizes considered; the THz range contains essentially tails of these signals. Figure 3(a) shows the dependence of the real part of the calculated mobility on the NC size for three particular frequencies in the THz range, which is accessible by our experiment. From these plots, we can conclude that the mobility values start to decrease significantly for NC sizes below 20 nm.

B. Effective conductivity

Effective (measurable) conductivity $\Delta\sigma$ of most structures can be calculated from the microscopic photoconductivity $\Delta\sigma_{\mathrm{mic}}$ inside NCs (obtained from a suitable microscopic model) using a simple expression [19,20,10],

$$\Delta\sigma = V\Delta\sigma_{\mathrm{mic}} + \frac{B\Delta\sigma_{\mathrm{mic}}}{1 + iD\Delta\sigma_{\mathrm{mic}}/\omega\varepsilon_0}. \qquad (6)$$

Here, V is the percolation strength of the photoconductive component. For small percolation strengths, we can define the coefficients B and D, which characterize the morphology of the nonpercolated parts of the sample, using the Maxwell-Garnett parameters K (shape factor) and s (filling fraction) as follows [10]:

$$B = \frac{\varepsilon_m(1 + sK) - \varepsilon(1-s)}{\varepsilon_m(s+K) + \varepsilon_b(1-s)} \qquad (7)$$

$$D = \frac{(1-s)}{\varepsilon_m(s+K) + \varepsilon_b(1-s)}, \qquad (8)$$
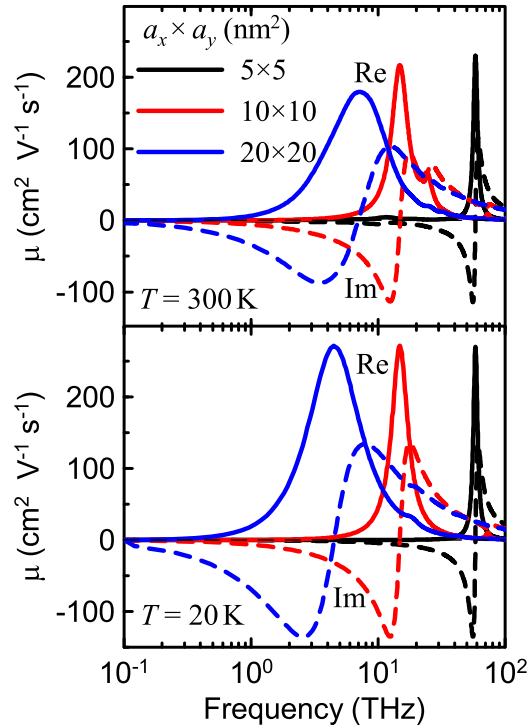
FIG. 2. Examples of THz and multi-THz mobility spectra calculated by the quantum mechanical approach for Si NC sizes $a_x \times a_y$ of 5×5, 10×10, and 20×20 nm^2 ($a_z = 4$ nm); dephasing time $1/\gamma = 60$ fs. Top: $T = 300$ K; bottom: $T = 20$ K; full lines: real part; dashed lines: imaginary part.

where ε_m is the permittivity of the SiO$_2$ matrix, ε_b is the background (ground-state) permittivity of the photoconductive Si NCs, and ε is the effective permittivity of the sample in the ground state. In this way, the conductivity mixing rules of our nanostructured composite are defined using well-established parameters.

The local microscopic conductivity is related to the mobility spectrum $\mu(\omega)$ derived on a quantum basis in the previous paragraph:

$$\Delta\sigma_{\text{mic}} = eN\mu, \qquad (9)$$

where e is the elementary charge and N is the local photocarrier density, which is proportional to the pump fluence. As shown in Fig. 3(a), μ *a priori* depends on the NC size d, and we keep this implicit dependence in mind. In our previous papers, we found it convenient to introduce the microscopic conductivity normalized by the photon pump fluence ϕ (see Ref. [20]),

$$\Delta\sigma_{\text{norm}} = \frac{\Delta\sigma_{\text{mic}}}{e\phi\alpha} = \frac{\alpha_{Si}}{\alpha}\xi\mu, \qquad (10)$$

where ξ is the quantum yield of the optical generation of mobile carriers, α_{Si} is the absorption coefficient of Si NCs, and α describes the mean absorption in the composite sample consisting of photoexcited and nonphotoexcited parts (it is the coefficient that enters the Lambert-Beer absorption law in the composite). The product $N_{\text{exc}} = \phi\alpha$ has the meaning of an average concentration of carriers in the composite.
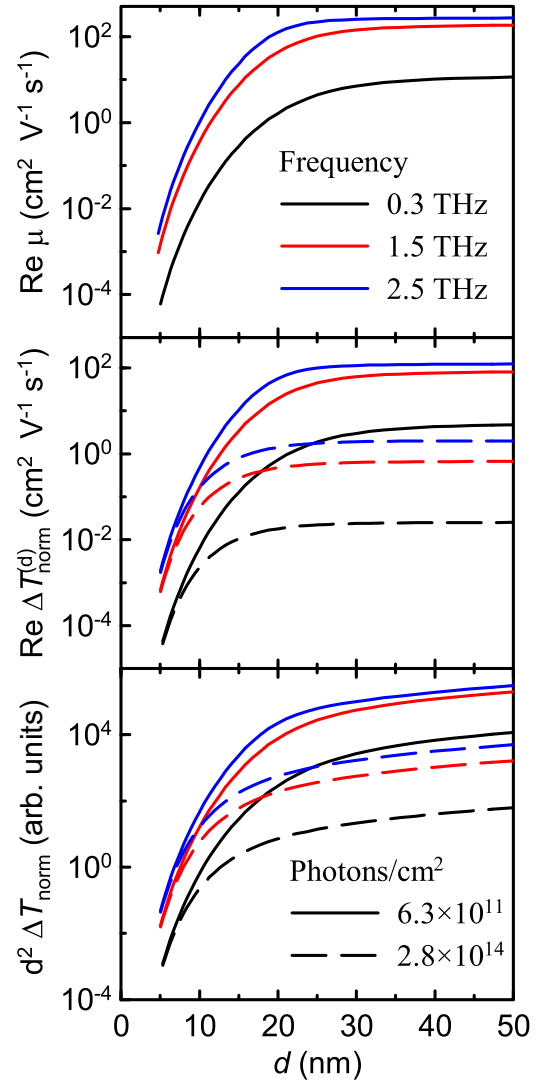

FIG. 3. (a) Real part of quantum mechanical mobility of Si NCs as a function of the NC in-plane size d ($a_x = a_y = d, a_z = 4$ nm) at three different frequencies and at 20 K. (b) Real part of normalized transient transmission ΔT_{norm} calculated from the data of the plot (a) with the help of Eq. (12) using typical parameters of our samples at two excitation fluences. (c) Weighted transient transmission $d^2 \times \Delta T_{\text{norm}}$ in arbitrary units (the same units for all the curves), which represents the real part of the THz signal per single nanocrystal with the given size.

C. Transient THz transmittance

Our experiment yields the spectra of transient transmittance $\Delta E/E$, where ΔE is the photoinduced (transient) part of the transmitted THz field and E is a reference field transmitted through the unexcited sample. We introduced the so-called normalized transmission function ΔT_{norm}, which has the dimension of the mobility and, in homogeneous samples, it has directly the meaning of the microscopic mobility [20],

$$\Delta T_{\text{norm}} = -\frac{(n_1 + n_2)}{z_0}\frac{1}{e\phi}\frac{\Delta E}{E}, \qquad (11)$$

where $n_1 = 1$ and $n_2 = 1.97$ are refractive indices of the media surrounding the sample (air and fused silica) and $z_0 = 377$ Ω

is the vacuum wave impedance. For a thin film sample (with thickness L), containing both percolated and nonpercolated photoconducting parts, where the optical pump is only partially absorbed, ΔT_{norm} is related to the photoconductivity as follows [20]:

$$\Delta T_{\text{norm}}^{(d)} = V[1 - \exp(-\alpha L)]\Delta\sigma_{\text{norm}} + B\frac{\ln(1 + Y_0) - \ln(Y_0 \exp(-\alpha L))}{Y_0}\Delta\sigma_{\text{norm}}, \quad (12)$$

where

$$Y_0 = \frac{iD}{\varepsilon_0 \omega}e\phi\alpha\,\Delta\sigma_{\text{norm}}. \quad (13)$$

The superscript (d) in Eq. (12) reminds us of the fact that this theoretical quantity depends on the dominant size of NCs through the confinement effects encoded into $\Delta\sigma_{\text{norm}}$. Finally, in order to take into account the distribution of NC sizes in a sample, we define the weighting of the transient THz signals coming from various NCs by their volume [10,23],

$$\Delta T_{\text{norm}} = \frac{\int_{d1}^{d2} \Delta T_{\text{norm}}^{(d)}\, w(d)\, \mathrm{d}\,d}{\int_{d1}^{d2} w(d)\, \mathrm{d}\,d}, \quad (14)$$

where $w(d)$ is the volumic density of NCs with the size d. Equations (11) and (14) constitute the primary link between the measured and calculated quantities.

Equation (14) is quite complex, and it is expected that the distribution of NC sizes may influence significantly the shape of the measured THz spectra. We provide the following discussion and show the curves in Fig. 3 in order to clarify the main trends in the variation of several important quantities with the NC size. In Figs. 3(b) and 3(c), we demonstrate the sensitivity of the standard THz spectroscopy to the conductivity processes in variously sized Si NCs. Figure 3(b) shows the normalized transmission $\text{Re}(\Delta T_{\text{norm}}^{(d)})$ calculated for the case when NCs with the given dimensions ($a_x = a_y = d, a_z = 4$ nm) have the same total *volume* in the sample independently of their size d. At low pump fluences (i.e., under conditions for which the depolarization fields are negligible), this quantity follows the behavior of the microscopic mobility μ plotted in Fig. 3(a). At high pump fluences [dashed lines in Fig. 3(b)], owing to the depolarization field effects, the drop in the normalized transmission observed for small NC dimensions ($d < 20$ nm) is less pronounced. It means that the range of a good experimental sensitivity is broadened and its lower end is shifted down to about a 10 nm size (note that ΔT_{norm} is a quantity normalized by the pump fluence; the raw measured signal $\Delta E/E$ will be appropriately upscaled by the value of ϕ for high fluences). The imaginary parts (not shown in the figures) are negative but exhibit analogous decrease of the absolute value for decreasing nanoparticle size. In Fig. 3(c), we plot the calculated product $d^2 \times \Delta T_{\text{norm}}^{(d)}$ as a function of NC size d normalized with respect to 50-nm-sized NCs. This weighted transient transmission function provides information about the signal coming from samples where NCs with the given size have the same *number*. In fact, the plot represents (in relative units) the THz photoconductivity signal per single NC. A dramatic decrease of the signal with the NC size in our quasi-two-dimensional (2D) system (which is enhanced due to the proportionality to d^2) is clearly observed. In standard

disordered 3D nanostructures, the signal of individual NCs is proportional to $d^3 \times \Delta T_{\text{norm}}^{(d)}$, i.e., its decrease towards small NCs will be even faster.

IV. RESULTS AND DISCUSSIONS

A. Fitting model

The multilayer samples, where the NC size is imposed by the layer thickness to some extent, offer *a priori* a better control over the NC size than in other 3D samples. However, it has been shown previously that the photoconductivity experiments can clearly detect larger Si clusters in this kind of sample and, consequently, that a significant distribution of sizes clearly does exist [10]. For this reason, in this paper we assume a continuous distribution of NC sizes following the log-normal law:

$$f_{\text{LN}}(d) = \frac{1}{d\,\delta\sqrt{2\pi}}\exp[-(\ln d/d_0)^2/2\delta^2],\, w(d) = d^2 f_{\text{LN}}(d), \quad (15)$$

where d is the in-plane diameter of the NCs, δ and d_0 define the width and the peak position of the distribution, respectively, and w is the volumic density of NCs entering Eq. (14). The mobility spectra of electrons moving in NCs described by the size distribution [Eq. (15)] are calculated by means of the quantum mechanical approach described above. Spectra for NC sizes between $d_1 = 4$ nm and $d_2 = 100$ nm were calculated with a 1 nm step in order to create a database of spectra densely covering the investigated range; subsequently, interpolation of the data was applied in order to operate with quasi-continuous series of data, as required by a fitting with Eq. (15). The spectra were calculated for 300 K and 20 K and for several dephasing times $1/\gamma$ in the range 30–120 fs. Based on the calculated $\mu(\omega)$, $\Delta T_{\text{norm}}^{(d)}$ is evaluated using Eq. (12) with the values of absorption coefficient α obtained from absorbance measurements, which are provided in Table I. We considered the percolation coefficient $V = 0$; indeed, we think that the dielectric percolation condition cannot be compatible with the quantum confinement model describing NCs with a defined relatively small size. The parameters B and D of the effective medium model are related to the sample morphology, and they are defined by Eqs. (7) and (8) with the shape factor $K_{\text{coh}} = 2$ and a filling fraction denoted s_{coh}. This term describes mostly coherent motion of electrons in NCs that dominantly contribute to the conductivity.

In addition to the coherent term, we consider that an additive incoherent contribution may exist. By this second contribution, we intend to take into account the conductivity of possibly existing considerably larger Si NCs and/or some percolated paths, which are predicted by TEM measurement in samples with $x \leqslant 0.5$. The incoherent character of this term (limited by a dominant scattering or other mechanism hindering coherent long-range transport) is inferred from the shape of experimental spectra [see Fig. 4]: (i) The real part of the conductivity in Si rich samples does not vanish at low frequencies, which implies the existence of a long-range conduction; (ii) for example, in polycrystalline Si layers with nearly micrometer-sized grains, the character of the *coherent*
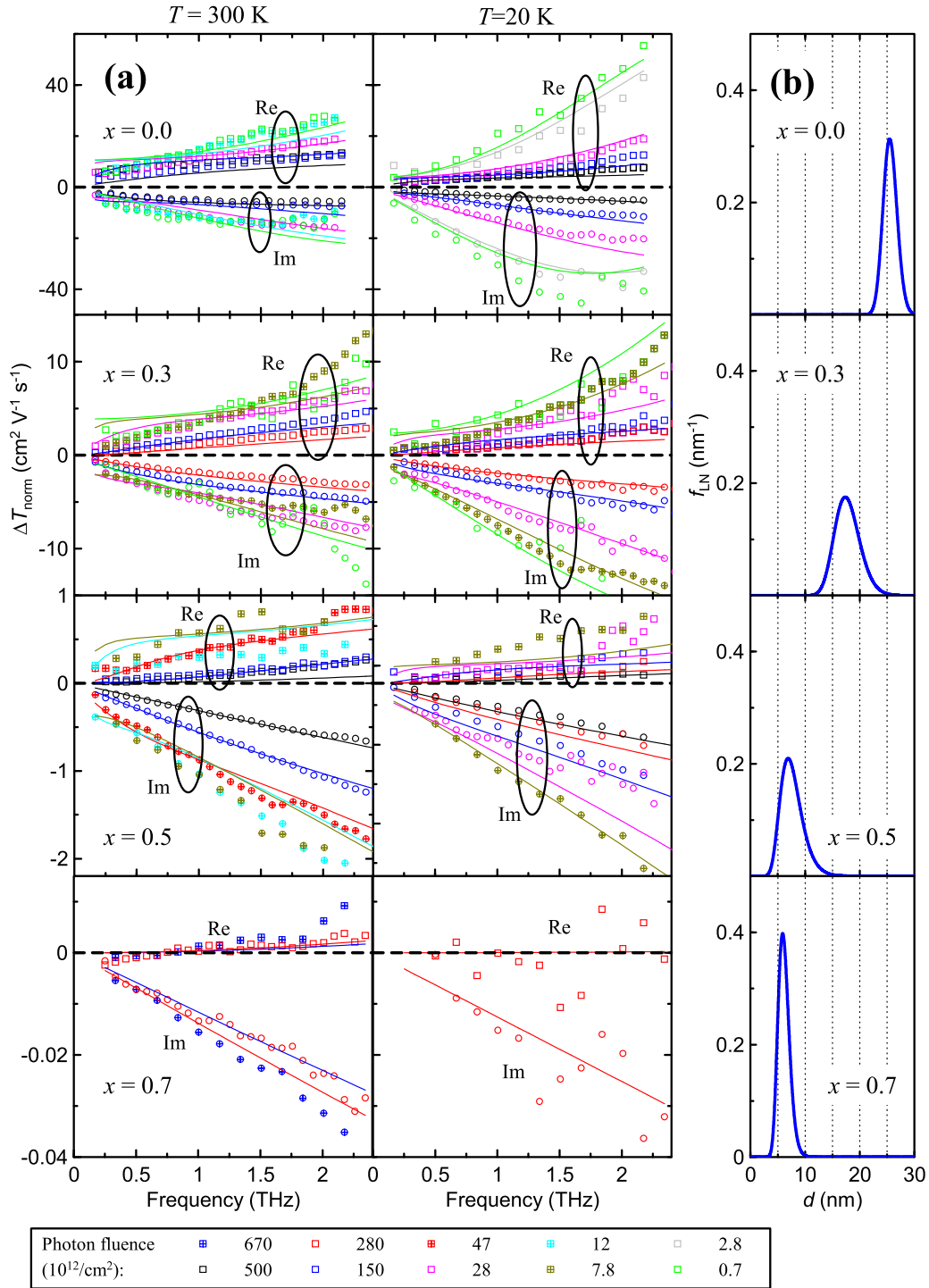
FIG. 4. (a) Normalized transient transmission spectra for samples 0.0, 0.3, 0.5, and 0.7 at room temperature and 20 K; pump–probe delay: 10 ps. Symbols: experimental data; lines: global fits of the data by Eq. (14); pump fluences are indicated in the legend. (b) Size distributions of NCs participating to the conductivity as obtained from the fits of experimental spectra.

response would be Drude-like with a higher magnitude and a significantly decreasing real part with frequency [24], which is clearly not the case here. As the character of the motion of these charge carriers is unknown, we assume here the simplest case of constant value of the real part of the mobility μ_{RT} for the RT and μ_{LT} for the LT. These inclusions are characterized by a filling fraction s_{inc}.

It has been shown that NCs with diameter $d \approx 4$ nm and smaller do not contribute to the response in the THz range. Hence the filling factor $s_{coh} + s_{inc}$ represents the part of Si NCs that can be detected by THz conductivity measurements. This sum can be smaller than the nominal value s presented in Table I; consequently, s_{coh} and s_{inc} are used as fitting parameters.

In total, we have six fitting parameters for each sample: $s_{coh}, s_{inc}, \mu_{RT}, \mu_{LT}, \delta$, and d_0, which should describe the complex spectra at both 300 K and 20 K and for a set of pump fluences spanning over nearly three orders of magnitude. We also tried to free the shape factor of inclusions participating to the incoherent contribution K_{inc}, which, in the case of sample SiO$_{0.0}$, significantly improves the fit when the value of K_{inc} differs from two. Consequently, we include also this possibility in our discussion.

B. Discussion

The model [Eq. (14)] was used to fit globally the experimental spectra, and the comparison can be seen in Fig. 4 for four samples (SiO$_{0.0}$, SiO$_{0.3}$, SiO$_{0.5}$, and SiO$_{0.7}$). The measured signal for sample SiO$_{0.7}$ was very weak; therefore, we were able to perform experiments with the highest excitation fluence only.

If we compare the RT results with those measured at 20 K for each sample, we find that no dramatic changes in the spectra are observed. This is explained by the quantum model: We observe a good match of the experiment with the fits both in the absolute values of mobilities and in roughly correct pump fluence dependence. We would like to stress that such an agreement cannot be achieved within the semiclassical Monte-Carlo modeling of the data: In this case, when the fits are approximately matched to the data at 300 K, the calculations highly overestimate the mobilities observed at 20 K [15].

The real part of the measured spectra is positive and grows with a frequency increase towards the lowest energy level of confined electrons. The imaginary part always decreases and has negative values: This is again a signature of the charge carrier confinement inside Si NCs and of the effective capacitive response of the sample. The effect of depolarization fields is clearly observed through a significant dependence of the spectra ΔT_{norm} on the excitation fluence density. An increase of the signal amplitude with an increase of Si content (decrease of values x) is due to an improved mobility related to a better connectivity of NCs leading to a larger average cluster size, as observed in Fig. 4(b). Indeed, Fig. 4(b) shows the NCs size distribution defined by Eq. (15), which follows from the fits. Clearly the distribution of conductive NCs shows a significant shift of its maximum towards smaller NCs when the Si content in the layers is decreased. The other parameters provided by the fitting procedure are summarized in Table I.

The THz spectra below 3 THz do not depend much on the dephasing factor γ. Note that the dephasing time $1/\gamma$ at RT in high quality Si single crystals reaches about 200 fs [25], while in polycrystalline Si films it may decrease typically down to about 60 fs [24] or to ~35 fs in the case of silicon on sapphire [5]. We verified that the spectra can be fitted with quite similar sets of parameters for the scattering times $1/\gamma$ ranging between 50 and 120 fs; however, for the scattering times of 30 fs or shorter, the quality of the fit becomes significantly worse. This is in agreement with our hypothesis of essentially coherent contribution of confined charge carriers in Si clusters described by the quantum model of the mobility.

At first glance the comparison of EF-TEM images and size distributions (see Ref. [12]) with the size distributions inferred from THz spectra may seem problematic. However, we think

that they present both a valuable and complementary tool of analysis of the behavior of the nanostructures. The TEM images provide information regarding the shape and size of inclusions, which are statistically most frequently encountered in the sample. However, their electrical connectivity cannot be determined from TEM images, and the percolation or nonpercolation of the system is only inferred from a geometrical proximity of several inclusions. In contrast, the THz spectroscopy provides a statistical image of inclusions that carry the conductivity of the sample. On one hand, very small inclusions feature a stronger confinement and a small volume per inclusion, which may lead to a very low contribution to the conductivity of such NCs; on the other hand, the carrier transport in the parts, which are considered to be percolated in TEM images, may be hindered by defects or internal structure of these parts.

The sample with $x = 0.0$ was reported to be percolated from the point of view of TEM [12]. However, at THz frequencies, it behaves like a polycrystalline Si such that the electrons feel an average confinement on the order of 25 nm. This can be put into contrast with our recent measurements of polycrystalline Si samples with the grain size of about micrometer, where the Drude-type response is clearly observed without any significant pump fluence dependence of the carrier mobility [24]. This means that in our current NC sample, quite large energy barriers separate the crystal grains and that the electrons cannot move freely among them. Note that in the related TEM image shown in Ref. [12], many contrasted objects with a typical size of the order of 25 nm can be really identified. The inclusion of the incoherent conductivity term systematically leads to large values of the shape factor ($K_{inc} > 20$), which represent a percolation of the system or sample morphology close to the percolation. This behavior could have been equivalently accounted for by a nonzero percolation strength term V.

In samples with $x = 0.3$ and 0.5, the distribution of conductive NCs progressively shifts to lower values and also the volumic filling fraction of the NCs participating to the THz conductivity drops to about 60–40%. The conductivity is essentially carried by NCs with the size distribution about 17 nm for $x = 0.3$ and about 7 nm for $x = 0.5$. There is still some non-negligible proportion of large NCs, which may be close to conductive percolation. Note that the width of the size distribution of sample SiO$_{0.3}$ is the largest, which means that in such a sample (nearly completely percolated from the point of view of TEM measurements), a rich variety of inclusion sizes and shapes can really develop. The size distribution becomes narrower again for $x = 0.7$, where the THz signal becomes quite weak as we approach the nominal size of NCs of 4.5 nm and crystals larger than 10 nm practically do not exist within the whole volume of the sample.

As to the incoherent contribution to the conduction, which has been tentatively added to the fitting procedure, very similar values of the RT and LT mobilities have been found among the samples. Systematically, $\mu_{RT} > \mu_{LT}$, indicating that this transport process is thermally activated (limited by some hopping steps or by energy barriers). In such a case, the real part of the mobility is typically increasing with increasing frequency (cf. description of the hopping mechanism in Ref. [15]). This could explain small discrepancies of the fits and experimental data in the lowest frequency region where the

fit overestimates the real part of the measured mobility due to the fact that we assume spectrally independent values of μ_{RT}. However, adding further parameters or particular models, able to describe this mobility decrease, would not lead to better understanding of underlying processes; therefore, we did not attempt this procedure. The most important conclusion here is that the incoherent part of the conduction is limited by energy-activated processes.

V. CONCLUSIONS

We developed a quantum approach to the calculation of the spectra of complex THz conductivity of NCs and showed that it can be successfully applied to the fitting and interpretation of temperature and pump fluence dependent photoconductivity spectra of ensembles of Si NCs. Our analysis was focused on samples with variable and technologically controlled content of silicon in quasi-2D layers.

We show that a careful analysis, based on formulas rigorously derived from the wave equation for THz waves in inhomogeneous photoexcited media, can provide a com-plementary picture of the NCs conductivity to TEM images. In particular, we were able to show that a broad distribution of NC sizes exists in the sample, and we identified the sizes, which contribute the most to the dynamical conductivity of the sample.

Sample $SiO_{0.0}$ with the largest Si content is close to the percolation, and the conductivity signal is driven by electrons in grains with a typical dimension of 25 nm; such objects are observed in TEM images. With decreasing content of Si, the size of NCs with the dominant contribution to the conductivity progressively decreases, and for a clearly nonpercolated sample $SiO_{0.7}$ the size of conducting NCs measured by THz spectroscopy becomes comparable to the thickness of SiO_x layers. This also proves the good control of the nanocrystalline size for oxygen rich samples.

[1] L. Pavesi and R. Turan, *Silicon Nanocrystals. Fundamentals, Synthesis and Applications* (Wiley-VCH, Wienheim, 2010).

[2] J. Bisquert, *Nanostructured Energy Devices: Equilibrium Concepts and Kinetics* (CRC Press, Boca Raton, 2015).

[3] N. Koshida, *Device Applications of Silicon Nanocrystals and Nanostructures* (Springer Science+Business Media, New York, 2009).

[4] A. Jane, R. Dronov, A. Hodges, and N. H. Voelcker, Trends Biotechnol. **27**, 230 (2009).

[5] D. G. Cooke, A. N. MacDonald, A. Hryciw, J. Wang, Q. Li, A. Meldrum, and F. A. Hegmann, Phys. Rev. B **73**, 193311 (2006).

[6] D. G. Cooke, A. N. MacDonald, A. Hryciw, A. Meldrum, J. Wang, Q. Li, and F. A. Hegmann, J. Mater. Sci.: Mater. Electron. **18**, 447 (2007).

[7] L. V. Titova, T. L. Cocker, D. G. Cooke, X. Wang, A. Meldrum, and F. A. Hegmann, Phys. Rev. B **83**, 085403 (2011).

[8] A. M. Hartel, D. Hiller, S. Gutsch, P. Löper, S. Estradé, F. Peiró, B. Garrido, and M. Zacharias, Thin Solid Films **520**, 121 (2011).

[9] S. Gutsch, D. Hiller, J. Laube, M. Zacharias, and C. Kübel, Beilstein J. Nanotechnol. **6**, 964 (2015).

[10] H. Němec, V. Zajac, P. Kužel, P. Malý, S. Gutsch, D. Hiller, and M. Zacharias, Phys. Rev. B **91**, 195443 (2015).

[11] J. Laube, S. Gutsch, D. Hiller, M. Bruns, C. Kübel, C. Weiss, and M. Zacharias, J. Appl. Phys. **116**, 223501 (2014)

[12] J. Laube, S. Gutsch, D. Wang, C. Kübel, M. Zacharias, and D. Hiller, Appl. Phys. Lett. **108**, 043106 (2016).

[13] F. L. Pedrotti and L. S. Pedrotti, *Introduction to Optics*, 2nd ed. (Prentice Hall, Englewood Cliffs, New Jersey, 1993).

[14] M. A. Green and M. J. Keevers, Prog. Photovolt: Res. Appl. **3**, 189 (1995).

[15] L. Fekete, P. Kužel, H. Němec, F. Kadlec, A. Dejneka, J. Stuchlík, and A. Fejfar, Phys. Rev. B **79**, 115306 (2009).

[16] T. Suzuki and R. Shimano, Phys. Rev. Lett. **103**, 057401 (2009).

[17] H. Němec, P. Kužel, and V. Sundström, J. Photochem. Photobiol. A **215**, 123 (2010).

[18] H. Němec, P. Kužel, and V. Sundström, Phys. Rev. B **79**, 115309 (2009).

[19] H. Němec, V. Zajac, I. Rychetský, D. Fattakhova-Rohlfing, B. Mandlmeier, T. Bein, Z. Mics, and P. Kužel, IEEE Trans. Terahertz Sci. Technol. **3**, 302 (2013).

[20] P. Kužel and H. Němec, J. Phys. D: Appl. Phys. **47**, 374005 (2014).

[21] M. P. Marder, in *Condensed Matter Physics* (Wiley, New York, 2000), pp. 625–627.

[22] J. Lloyd-Hughes and T.-I. Jeon, J. Infrared Milli. THz. Waves **33**, 871, (2012).

[23] V. Zajac, H. Němec, C. Kadlec, K. Kůsová, I. Pelant, and P. Kužel, New J. Phys. **16**, 093013 (2014).

[24] P. Pikna, V. Skoromets, C. Becker, A. Fejfar, and P. Kužel, Appl. Phys. Lett. **107**, 233901 (2015).

[25] C. Jacoboni, C. Canali, G. Ottaviani, and A. A. Quaranta, Solid-State Electron. **20**, 77 (1977).